

Towards a Universal Veering Profile for Turbulent Ekman Flow at arbitrary Reynolds number - Part 2

LES and DNS of Turbulent Ekman Flow

hauke-zrick

Draft August 18, 2023

Abstract

We use an analytical formulation for the profiles of stream- and span-wise velocity in turbulent Ekman flow and large-eddy simulations to analyze the properties of turbulent Ekman flow. We show a comparison of a turbulent Ekman flow of $Re_D = 1\,600$ simulated by DNS and LES.

1 Introduction

[start introduction with relevance of LES or relevance of Ekman flow?]

Large Eddy simulations (LES) are widely used to model turbulent flows in the atmospheric boundary layer. This includes the simulation of wind turbines or wind farms as well as wind turbine wakes and wind farm cluster interactions [Porté-Agel et al., 2011, Mehta et al., 2014, Breton et al., 2017]. Furthermore, LES deliver simulations of flows over complex environments like mountainous or urban areas [Stoll et al., 2020, García-Sánchez et al., 2018]. All these applications have in common that they are situated in the lower part of the atmospheric boundary layer on the rotating earth. This part of the atmospheric boundary layer is characterized by logarithmic increase of the wind speed above the surface layer and a change of wind direction above in the so called Ekman layer. In reality, the turbulent boundary layer is usually capped by a temperature inversion. The information how exactly the wind speed and the wind direction change with height is of great importance for wind-power forecasting Optis et al. [2014].

In part I of this publication, we presented a generic profile of wind direction and speed in turbulent Ekman flow. Foundations: Csanady [1967], Tennekes [1973], Spalart [1989]

The most simple version of this kind of boundary layer is the turbulent Ekman flow. It is a horizontally homogeneous, statistically stationary boundary layer flow over a rotating flat surface under neutral stratification, characterized by only the geostrophic wind G , the Coriolis parameter f and the kinematic viscosity ν . It can serve as a simple model of the atmospheric boundary layer since it exhibits the key characteristics shaping the real atmosphere: the logarithmic layer and the Ekman spiral. Hence, the investigation of this case is suited to learn about the fundamental properties of the atmospheric boundary layer. Near the surface, viscous forces dominate the flow. In the middle part, the velocity profile has a logarithmic shape which passes over into an Ekman spiral. The investigated flow is truly neutrally stratified, which means that the potential temperature is constant for the whole domain. This does not imply unlimited growth of the boundary layer height – the boundary layer height evolves from intrinsic Ekman dynamics [reference?].

An assumption regarding the use of LES is that the first order velocity profiles are reproduced quite accurately while higher moments are not fitting observations very well (reference?). With the comparison of LES to a theoretical solution we investigate for which conditions this assumption is true.

[Before talking about the Reynolds number, it would be useful to introduce the concept of scale separation and briefly discuss it with respect to LES.]

We investigate three different Reynolds numbers Re_D : 1 600, 150 000, and 1 000 000, where $Re_D = GD/\nu$ and $D = \sqrt{2\nu/f}$, $Re_D = G/\sqrt{\frac{1}{2}\nu f}$. While the low-Re case ($Re_D = 1600$) is also investigated by DNS (cf. part 1 of this study), $Re_D = 10^6$ corresponds to the scale separation found in typical atmospheric boundary layers. This approach raises our confidence in the LES results to a new level for the direct comparison with a resolving simulation. And it allows us to extend the insight to atmospheric scale where a direct approach is clearly infeasible for computational constraints.

Neutral Ekman layer with LES: Esau [2004], Jiang et al. [2018]

Limits of coarse resolution

This paper investigates the mean velocity profiles of the turbulent Ekman flow from moderate to high Reynolds numbers using the formulation from part I and LES.

The turbulent structures in boundary layers of high Reynolds numbers extend over a large range of scales. For the description of their vertical mean profiles, inner units ($z^+ = zu_*/\nu$, $U^+ = U/u_*$) and outer units ($z^- = z/\delta$, $U^- = U/G$) are used. At the lower boundary, the x-axis of the inner units is aligned with the shear stress, whereas the x-axis of the outer units is aligned with the geostrophic wind. The angle between both axes is called α_* . [Orientation of axes strictly connected to inner/outer units?]

The content is structured as follows. Section 2 provides a complete mathematical description of the turbulent Ekman layer's velocity profiles. A description of the simulated cases and the numerical set-up is given in section 3, followed by the presentation of results in section 4. We conclude in section 5.

2 A Universal Velocity Profile for the Turbulent Ekman Layer

The universal velocity profile for the turbulent Ekman layer is derived and extensively discussed in part I of this paper. In this chapter, we give a brief but complete mathematical description of the velocity profiles.

2.1 Total profile

As frame of reference we use the coordinate system Oxyz with Ox in the direction of the surface stress and Oy in the span-wise direction normal to Oxz. The profile of the stream-wise component of the velocity is separated into three layers, which are the viscous layer U_{visc} , the logarithmic layer U_{log} , and the Ekman layer U_{EK} . U_{visc} and U_{log} are matched by their formulation and combined to U_{inner} . The span-wise component of the velocity is separated into two layers, namely the inner layer V_{inner} , and the Ekman layer V_{EK} . The smooth transition between consecutive layers is achieved using a transfer function:

$$w_* = \frac{1}{2} \left(\operatorname{erf} \left[\sigma_T \log \left(\frac{z}{z_T} \right) \right] + 1 \right), \quad (1)$$

where σ_T is a transition scale that defines the width of the transition and z_T is the height of the transition, where the upper and the lower layer equally contribute to the velocity ($w_*(z_T) = 0.5$).

$$U = (1 - w_{outer})U_{inner} + w_{outer}U_{EK}, \quad (2a)$$

$$V = (1 - w_{outer})V_{inner} + w_{outer}V_{EK}. \quad (2b)$$

2.2 Drag-Law

The geostrophic drag $Z \equiv u_\star/G$ and the angle between the shear stress and the geostrophic wind α_\star are two key parameters of the Ekman flow. They can be estimated using a semi-empirical drag-law based on Spalart [1989], which describes them as functions of only the Reynolds number:

$$\frac{G}{u_\star} \cos \phi^\star = \frac{1}{\kappa} \log Re_\tau + C - A_r, \quad (3a)$$

$$\sin \phi^\star = A_i \frac{u_\star}{G}, \quad (3b)$$

$$\alpha_\star = \phi^\star - \frac{C_5}{Re_\tau}, \quad (3c)$$

with $Re_\tau = \frac{Re_D^2 u_\star^2}{2 G^2}$, $\kappa = 0.416$, $A_r = 4.80$, $A_i = -5.57$, $C = 5.4605$, $C_5 = -57.8$. This law is in excellent agreement with DNS in the range $400 \leq Re_D \leq 1600$ as demonstrated by Ansorge and Mellado [2014].

2.3 Profiles in Outer Layer

Above the boundary layer, the horizontal pressure gradient is balanced by the coriolis force and the wind speed equals the geostrophic wind G . For the stationary case, the horizontal equations of motion are solved by

$$U_{EK} = G + A e^{-\tilde{z}} \cos \tilde{z}, \quad (4a)$$

$$V_{EK} = -A e^{-\tilde{z}} \sin \tilde{z}, \quad (4b)$$

where the x-axis is aligned with the geostrophic wind and $A = 8.4u_\star$, $\tilde{z} = (z - z_r)/D_E$, $z_r = 0.12\delta$, and $D_E = 3\delta/4\pi \approx 0.24\delta$. The parameters are deduced from DNS. The transition from the logarithmic layer to the Ekman layer is located at $z_T^- = 0.3 - 120/Re_D$ [in script at 0.28-2.25*np.sqrt(1./re)] with a transition scale of $\sigma_T = 2$ for the stream-wise velocity.

2.4 Shear-Aligned Velocity

In the viscous sublayer, the span-wise velocity is close to zero and the shear-aligned velocity is described by the law of the wall:

$$U^{\alpha_\star+} = z^+, \quad (5)$$

(the index α_\star indicates the alignment with the direction of the shear stress). Around $z^+ = 5$, the velocity is beginning to deviate from its linear profile and the buffer layer forms the transition between viscous layer and logarithmic layer. From the surface up to the buffer layer, the stream-wise velocity is described by

$$U_{visc}^{\alpha_\star+} = \frac{z^+}{1 + c_1(z^+)^2} + (c_2 z^+ - a_{match}) \frac{1 + \tanh[0.2(z^+ - 22)]}{2} + c_3 e^{-c_4(z^+ - 22)^2}. \quad (6)$$

With $c_1 = 0.00185$, $c_2 = 0.195$ [adapt c_2 ?], $c_3 = 0.4$, $c_4 = 0.35$. The coefficient $a_{match} = 3.5727$ is chosen to match the u-profile in the logarithmic layer above at $z^+ = 40$.

The logarithmic region of the stream-wise velocity is

$$U_{\log}^{\alpha_\star+} = \frac{1}{\kappa} \log z^+ + C, \quad (7)$$

with the von-Kármán constant $\kappa = 0.416$, and $C = 5.4605$. The lower part of $U^{\alpha*+}$ is described by

$$U_{inner}^{\alpha*+} = \begin{cases} U_{visc}^{\alpha*+}, & z^+ < 40, \\ U_{log}^{\alpha*+}, & z^+ > 40. \end{cases} \quad (8)$$

The inner profile is then blended to the Ekman profile using eq. 2 with $\sigma_T = 2$ and $z_T^- = 0.28 - 2.25\sqrt{1/Re_D}$.

2.5 Span-wise Velocity

In the viscous layer, the shear-aligned span-wise velocity is described as

$$V_{visc}^{\alpha*} = \frac{G}{\delta^+} v_{ref} (w_v z^+ - 1 + \exp[-w_v z^+]). \quad (9)$$

The choice of $v_{ref} = 18.85$ and $w_v = 0.2353$ leads to excellent agreement with the DNS data.

Above the viscous layer a log-like transition to the Ekman layer is modeled by

$$V_{log}^{\alpha*} = \frac{G}{\delta^+} (a_{log} + b_{log} \log(z^+) + c_{log} z^+). \quad (10)$$

A smooth transition to V_{visc} at $z^+ = 10$ and the condition $V_{log}(z^- = 0.3) = V_{EK}(z^- = 0.3) =: v_{03}$ lead to

$$c_{log} = \frac{v_{03} - v_{10} - d_{10} z_{10} \log(z_{03}/z_{10})}{z_{03} - z_{10}}, \quad (11)$$

$$a_{log} = v_{10} - d_{10} z_{10} \log z_{10} + c_{log} z_{10} (1 - \log z_{10}), \quad (12)$$

$$b_{log} = (d_{10} - c_{log}) z_{10}. \quad (13)$$

Here, $d_{10} = 4.01$, $v_{10} = 27.3$. Because of the **Re** dependence of V_{EK} , v_{03} also depends on **Re**. $V_{log}^{\alpha*}$ is blended into V_{EK} using eq. 2 with $\sigma_T = 2$ and $z_T^- = 0.28 - 2.25\sqrt{1/Re_D}$.

2.6 Profile

[How detailed should we explain this in Part II?] An example of the velocity profiles according to the above mathematical description is given in Fig. 1. In the viscous sublayer, the shear-aligned component U^+ increases linearly with height up to the buffer layer between $z^+ \approx 5$ and $z^+ \approx 30$, where it transitions into the logarithmic layer. Then, U^+ increases logarithmically up to the Ekman layer and reaches its supergeostrophic maximum. Above, it decreases to its geostrophic value. The length of the logarithmic layer increases with **Re**. The spanwise component V^+ remains close to zero up to the middle of the logarithmic layer, where the transition to the Ekman layer takes place ($z^- \approx 0.28 - 2.25\sqrt{1/Re_D}$). The profiles of V^+ of all Reynolds numbers have a similar shape but are shifted in z^+ . The similar V^+ and the growth of U^+ leads to a smaller angle α_* between surface shear stress and geostrophic wind for higher **Re**, which is visible in the hodograph.

3 Case description and numerical set-up

3.1 Settings

An incompressible, turbulent Ekman flow over a flat rotating plate is simulated for three different Reynolds numbers $Re_D = 10^3; 1.5 \times 10^5; 10^6$, hereafter *Re1*, *Re2*, and *Re3*, respectively. The key input parameters of the three cases are presented in table 1.

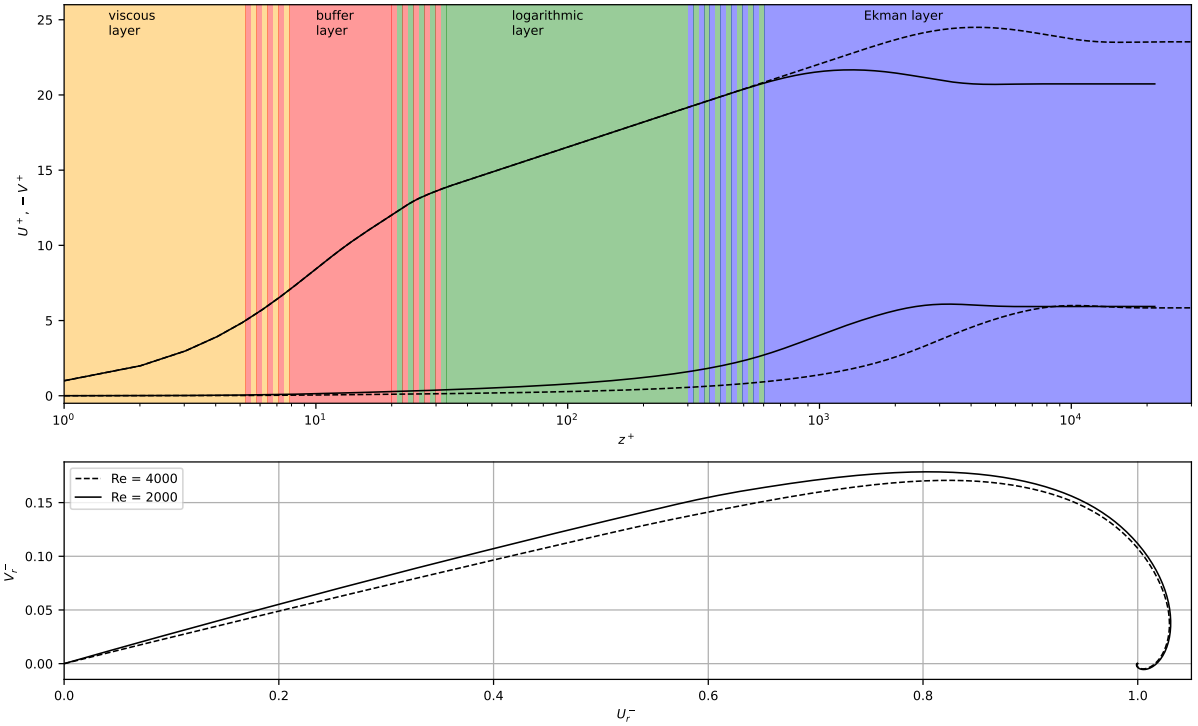


Figure 1: a) Theoretical shear-aligned velocity profile ($U^+, -V^+$) of the turbulent Ekman flow for $Re_D = 2000$ (—) and $Re_D = 4000$ (----) and the different layers (colors). b) Hodograph of the geostrophy-aligned velocity components

Table 1: Key parameters of the simulated cases. f , ν , and G are input parameters, while u_* , α_* , and $\delta = u_*/f$ are resulting properties of the flow according to Spalart [1989]

Name	Re_D	Re_τ	f [s $^{-1}$]	ν [m 2 s $^{-1}$]	G [ms $^{-1}$]	u_* [ms $^{-1}$]	α_* [$^\circ$]	δ [m]
Re1	1.6×10^3	3.0×10^3			0.0438	0.00211	16.8	21.1
Re2	1.5×10^5	7.3×10^6	10^{-4}	1.5×10^{-5}	4.108	0.1048	8.5	1048
Re3	1×10^6	2.2×10^8			27.39	0.5785	7.0	5785

Table 2: Simulations and grid parameters: ReX stands for one of the Reynolds numbers Re1, Re2, and Re3. Δ is the grid cell size, $\delta = u_*/f$ is the boundary layer height, n_i is the number of grid cells in the direction Oi, L_x and L_z are the domain sizes in the horizontal and vertical direction, respectively

Name	Δ/δ	n_x	n_y	n_z	L_x/δ	L_z/δ
ReX_50	1/50	192	192	128	3.84	5.0
ReX_100	1/100	384	384	216	3.84	4.5
ReX_150	1/150	576	576	288	3.84	3.7
ReX_200	1/200	768	768	384	3.84	4.1
ReX_dyn	1/200	768	768	384	3.84	4.1

The domain is rotating around the z-axis with an angular velocity such that the Coriolis parameter is $f = 10^{-4}$, a value representative of mid-latitude synoptic systems. The stratification of the flow is truly neutral, i.e., the potential temperature $\Theta = \text{const.}$ for the whole domain. At the upper boundary, a no-penetration boundary condition is used and the horizontal components of the wind are forced to equal the geostrophic wind through a Dirichlet-type boundary condition. At the bottom, a constant flux layer is assumed and Monin-Obukhov similarity theory (MOST) is used to calculate the surface momentum fluxes $\overline{u''w''}_0$ and $\overline{v''w''}_0$.

To study the effect of resolution on the simulations, four different grid resolutions are chosen for each Reynolds number case. The grid cell size Δ is around $\delta/50$, $\delta/100$, $\delta/150$, and $\delta/200$ for a coarse, two medium, and a fine resolution, respectively (see table 2).

The grid spacing inside the boundary layer is isotropic up to the height $z = 1.3\delta$. Aloft, the grid spacing along Oz is stretched by 3% per grid point until a maximum spacing of $(\Delta z)_{\max} = 6\Delta x$. The number of vertical grid points is chosen such that $L_z \geq 3\delta$. Different domain heights are caused by numerical requirements of the FFT-solver. Above two thirds of the total domain, Rayleigh damping is active to avoid reflections from the upper boundary.

In part I of this publication, the DNS of low Reynolds number simulations ($Re_D \leq 1\,600$) have a horizontal domain length of $L_x = 0.54\Lambda_{Ro}$ or $L_x = 1.08\Lambda_{Ro}$, where $\Lambda_{Ro} = G/f$ is the Rossby radius. For these Reynolds numbers, u_*/G is around 0.05 so $L_x = 0.54G/f \approx 10u_*/f = 10\delta$. However, u_*/G decreases with increasing Reynolds number and is around 0.02 for $Re_D = 10^6$. A domain size of half the Rossby radius would then extend to $L_x \approx 25\delta$. Such a large domain would imply immense computational costs. Spalart et al. [2008] used a horizontal domain of $L_x = 2\delta$, arguing that this length include the largest outer-layer eddies according to Csanady [1967]. During a sensitivity test of the domain size we observed that simulations with domain sizes $L \geq 4\delta$ often tend to accumulate turbulence kinetic energy in the upper half of the the boundary layer. This TKE increases over several T_{io} with energy mostly on the scale of the domain size. Such a development was not observed in the DNS. We could successfully avoid such a behaviour by using a domain of size $L = 3\delta$ in combination with a shifted periodic boundary condition in y-direction, as described by Munters et al. [2016]. Although for the Ekman flow the direction of the mean flow is only aligned with the x-direction of the grid near the surface, a shift of the boundary condition by $L/3$ significantly helped to suppress the accumulation of TKE in the upper half of the boundary layer. [leave out discussion of Rossby radius in paragraph above?]

In LES, the turbulent transport on the subgrid scale needs to be modeled by a subgrid-scale model (SGS model). The model code of PALM (PArallelized Large-eddy simulation Model, Maronga et al. [2020a]) offers two different SGS models: a 1.5-order closure after Deardorff [1980] and a dynamic closure after Heinz [2008]. For most of the simulations, the 1.5-order closure is used, but the simulations with the smallest grid cell size are repeated using the dynamic closure for comparison.

The equations are integrated using a 3rd-order low-storage Runge-Kutta method. For scalar advection a 5th-order Wicker-Skamarock scheme is employed. A comprehensive description of the LES model is given by Maronga et al. [2020a].

3.2 Viscosity and roughness length

In LES, one postulates that a sufficient part of the largest eddies (from a spectral perspective) is resolved so as to represent the non-linear effects of turbulent mixing. Below these resolved scales, turbulence is modelled as a more or less isotropically acting diffusive agent through a closure model (Dynamic, Deardorff, see above). Consequently, molecular friction is not considered directly, but only by virtue of a turbulence model that links the resolved scales and the dissipative scales. In their seminal works on the spectral energy transfer in homogeneous isotropic turbulence, Kolmogorov and Obukhov (Kolmogorov [1941], Obukhov [1941]) showed that the rate of energy transfer across the spectrum is in fact a constant implying that the rate of transfer across the cut-off scale in LES does not depend on the magnitude of the viscous scale, presupposed that (i) the cut-off scale of the LES is well within the inertial range and (ii) that the LES turbulence is approximately isotropic and homogeneous at the smallest resolved scales. This implies that an LES turbulence closure need not carry explicit information on the Reynolds number or viscosity of the flow.

However, the simulation of flows with relatively low \mathbf{Re} or very high resolution leads to results where the closure model yields eddy viscosities that are far below the assumed molecular viscosity $\nu = 1.5 \times 10^{-5} m^2/s$. The eddy viscosity in PALM is $K_m = c_0 \Delta \sqrt{e}$, where $c_0 = 0.1$ for the closure according to Deardorff [1980], Δ is the grid size and e is the SGS-TKE, calculated by a prognostic equation. Obviously, very low e as well as fine resolution can lead to $K_m < \nu$. When this is the case, ν cannot be ignored anymore. Thus, instead of only the modeled eddy viscosity we also consider the contribution of ν to the total viscosity of the flow, so $K_m = c_0 \Delta \sqrt{e} + \nu$. The governing equation of the velocity components in PALM reads

$$\frac{\partial u_i}{\partial t} = -\frac{\partial u_i u_j}{\partial x_j} - \epsilon_{ijk} f_j u_k + \epsilon_{i3j} f_3 u_{g,j} - \frac{1}{\rho_0} \frac{\partial \pi^*}{\partial x_i} + \frac{\partial}{\partial x_j} \left(K_m \left(\frac{\partial u_i}{\partial x_j} + \frac{\partial u_j}{\partial x_i} \right) \right) \quad (14)$$

for a neutrally stratified flow. In the limit of either very well resolved simulations or very low \mathbf{Re} (or both) we get $K_m \approx \nu$, so the last term on the right hand side of eq. 14 becomes $\nu \frac{\partial^2 u_i}{\partial x_j^2}$, which complies with the Navier-Stokes equations for an incompressible fluid.

In contrast to the interior closure of the LES where the direct effect of ν is of small relevance compared to the eddy viscosity—at least for high \mathbf{Re} —, this is not true for the viscous effects related to roughness which act in immediate vicinity to the surface. Here, instead of a no-slip condition at the bottom, a constant flux layer is usually assumed below the first grid point and the Monin-Obukhov theory is used to compute the friction velocity and the stresses at the first half grid point (where the horizontal velocities are located):

$$u_* = \frac{\kappa(U^2 + V^2)^{0.5}}{\ln(z/z_0)}, \quad (15)$$

$$-\overline{u''w''}_0 = \frac{\kappa U u_*}{\ln(z/z_0)}. \quad (16)$$

We immediately see that the viscosity is taken into account indirectly by choosing the roughness length z_0 when considering the law of the wall for a smooth surface:

$$u^+ = \frac{1}{\kappa} \ln(z^+) + C^+ = \frac{1}{\kappa} \ln \left(\frac{z^+}{z_0^+} \right). \quad (17)$$

This leads to

$$z_0^+ = \exp(-\kappa C^+), \quad (18)$$

and for an aerodynamically smooth flow, $z_0^+ = 0.1031$ (using the same values as in eq. 7). This is known to be the minimal roughness length of a turbulent boundary layer (see e.g. Kraus [2008]). The roughness length in SI-units

$$z_0 = z_0^+ \frac{\nu}{u_*} \approx 0.1 \frac{\nu}{u_*} \quad (19)$$

hence depends on the viscosity of the fluid, which means that the choice of z_0 implies a particular value for the viscosity ν .

Typically, a constant flux layer is assumed below the first grid point so that the stresses $\overline{u'w'}$ and $\overline{v'w'}$ can be calculated using MOST. It is assumed that the height of the first grid point lies inside of the logarithmic layer of the flow. Again, the limit of low **Re** and high resolution requires adaptations to the boundary condition. In the case of very fine resolution, the first grid point might fall into the buffer layer or even the viscous layer of the flow, so the equations of MOST are no longer adequate to calculate the local stress. To avoid that, we follow the recommendation of Kawai and Larsson [2012] to use horizontal velocity from a higher layer z_{sl} to compute the mean stress in the constant flux layer. Furthermore, we adopt the boundary condition suggested by Maronga et al. [2020b] and use the domain averaged velocities:

$$u_{*,mean} = \frac{\kappa \langle u_h(z_{sl}) \rangle}{\ln(z_{sl}/z_0)}, \quad (20)$$

where u_h is the absolute of the horizontal velocity and the angle brackets mean the horizontal average over the whole domain. The mean stress is then used as a boundary condition at the first grid point ($z = z_1$). It is distributed locally to the stresses in x- and y-direction via

$$\overline{u'w'}_0(x, y, z_1) = -u_{*,mean}^2 \frac{u(x, y, z_1)}{\sqrt{\langle u \rangle^2(z_1) + \langle v \rangle^2(z_1)}}, \quad (21)$$

and accordingly $\overline{v'w'}_0$. This way, the domain average of the stress components yield the total stress of eq. 20 ($u_{*,mean}^2 = \sqrt{\langle u'w' \rangle^2 + \langle v'w' \rangle^2}$). As reference height we use $z_{sl}^- \approx 0.1$. By using this higher reference height for the boundary condition we solve two problems: we ensure that the reference height is inside of the logarithmic layer and we use a velocity where the flow is much better resolved than close to the surface.

The initial profile of the flow is calculated by a 1d-model with a Reynolds-average based turbulence parametrization. At the beginning of the 3d run, random perturbations are imposed to the velocity field to trigger the evolution of turbulent eddies. The resulting imbalance between pressure force and Coriolis force results in an inertial oscillation of the period $T_{io} = 2\pi/f$, where a part of the flow's mean kinetic energy commutes between U- and V-component. The oscillation slowly decays over time and eventually vanishes. In order to obtain reliable profiles, we use a spin-up time of 1.5 T_{io} and perform a horizontal domain average over 2 T_{io} .

4 Results

In this chapter, we compare the results from the LES to the theoretical bulk parameters and velocity profiles and discuss the dynamics of the turbulent flow in LES.

4.1 Bulk parameters

The ratio of u_* to the theoretical value $u_{*,th}$ resulting from the simulations are shown in Tbl. 3. All values are close to one, while the strongest deviations are observed for the coarsest simulations. A slight dependence on the resolution can be observed for Re1, as u_* steadily approaches $u_{*,th}$ with increasing resolution. For Re2 and Re3, all but the coarsest resolution nearly exactly match the theoretical value. The choice of z_0 and the geostrophic wind G determine the

Table 3: Simulation results

Name	Δ^+	$u_\star/u_{\star,th}$	$\alpha_\star/\alpha_{\star,th}$	κ_{LES}	$z_{0,LES}/z_0$	δ_{95}/δ
Re1_50	59	1.021	0.9	-	-	0.71
Re1_100	30	1.008	0.92	0.52	0.14	0.66
Re1_150	20	1.004	0.93	0.48	0.33	0.64
Re1_200	15	1.003	0.95	0.46	0.47	0.62
Re1_dyn	15	1.002	0.94	0.43	0.78	0.58
Re2_50	1.5×10^5	1.008	0.86	-	-	0.77
Re2_100	7.3×10^4	1.001	0.93	0.53	0.02	0.66
Re2_150	4.9×10^4	1.000	0.97	0.47	0.15	0.60
Re2_200	3.7×10^4	1.000	0.99	0.44	0.49	0.59
Re2_dyn	3.7×10^4	1.000	0.99	0.42	1.01	0.55
Re3_50	4.5×10^6	1.007	0.89	-	-	0.76
Re3_100	2.2×10^6	1.001	0.93	0.53	0.01	0.65
Re3_150	1.5×10^6	1.000	0.96	0.47	0.07	0.60
Re3_200	1.1×10^6	1.001	0.99	0.44	0.33	0.59
Re3_dyn	1.1×10^6	1.000	0.99	0.43	0.62	0.56

magnitude of u_\star in a non trivial way. From a top perspective, the horizontal velocity increases from its geostrophic value to the supergeostrophic maximum and then decreases with height. The horizontal mean velocity at $z^- \approx 0.1$ is used to calculate u_\star according to eq. 20. It is remarkable that the choice of $z_0^+ = 0.1031$ leads to a value of u_\star very close to the prediction by semi-empirical considerations (cf. Spalart [1989]). These considerations include a specific relation $Z_\star = G/u_\star$ which is unique for each Reynolds number Re_D .

Another key parameter of the Ekman flow is the angle α_\star between the negative surface shear stress and the geostrophic wind. For the LES, we define α_\star as the angle between the mean wind vector at the first grid point and the vector of the geostrophic wind: $\alpha_\star = \tan^{-1}(\langle v_1 \rangle / \langle u_1 \rangle) - \tan^{-1}(V_G/U_G)$. Table 3 shows that all LES yield an α_\star smaller than the theoretical value $\alpha_{\star,th}$. In general, we observe an increase of α_\star with resolution. The finest resolution of Re_2 and Re_3 even reach 99% of the theoretical value while $Re1_200$ only reaches 95%. However, Fig. 2 shows that this is not caused by poor quality of the simulation since all of the simulations of $Re1$ follow the theoretical hodograph quite closely and even overestimate the angle at the respective height by a little. In contrast to the higher Re , the veering of the wind vector still continues in the lower parts of the boundary layer. So for the low Re case, the general trend of a higher α_\star with finer resolution is caused by the approach of the final α_\star with decreasing height of the first grid point.

4.2 Logarithmic layer stream-wise velocity

Figure 3 shows the velocity profiles from the LES and the theoretical profiles for all Re . In general, the velocity profiles of the LES agree quite well with the theoretical profiles. The course of the theoretical Ekman layer is matched closely and the simulations show a logarithmic layer for the U-component. For $Re1$, the lowest grid points fall into the buffer layer, which is visible as the curved course of the U-component below the logarithmic layer. The best resolved simulation with Deardorff-closure even seems to follow the course of the upper part of the buffer layer but with a resolution of $\Delta^+ = 15$ this is likely to be a coincidence. The lowest points of the LES of the higher Re fall into the logarithmic layer. Hence, for no simulation the viscous sublayer and the buffer layer are sufficiently resolved or even in the range of the vertical grid points of the LES and thus cannot be compared.

The most obvious deviations can be seen near the surface, where the simulations show several

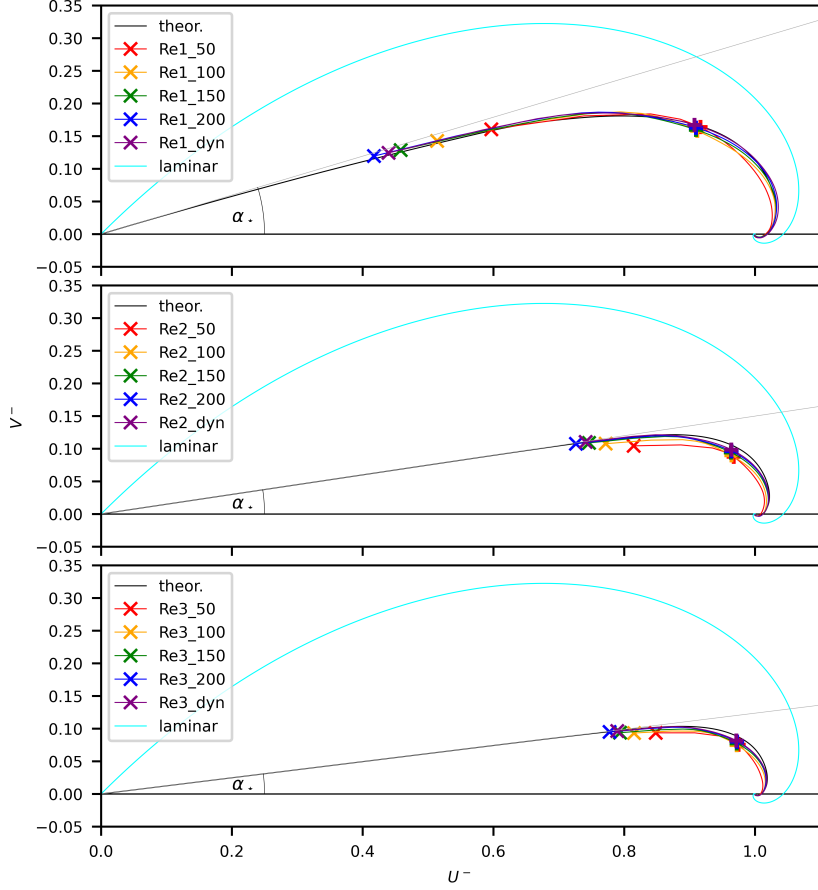


Figure 2: Geostrophy aligned hodographs of the LES in comparison to the theoretical and laminar hodographs. A \times indicates the first grid point of the LES. At the points marked with $+$, the velocity is used to determine u_* .

kinks in the velocity profile. This typical feature of LESs is the log-layer mismatch, which is a deviation from the law of the wall in mean velocity and gradient for the first grid points above the bottom. These deviations arise from a competition between the scales u_* and z and other velocity and length scales introduced by the discretization of the dynamical system [Mason and Thomson, 1992, Brasseur and Wei, 2010]. In other words, at the lower boundary, the relevant eddies are too small to be resolved by the grid and their contributions to the flow have to be modeled. Especially the vertical component is massively restricted by the non-permeability of the wall, known as blocking effect. However, the SGS-model assumes isotropic turbulence, which is not the case on the grid scale near the wall.

In the logarithmic region, the profile of the u -component should follow the logarithmic law of eq. 7. Ideally, the slope in a logarithmic plot would be $1/\kappa$. Figure 4 shows the Kármán measure $\kappa = (z^+ \partial U^+ / \partial z^+)^{-1}$, which is a constant inside of an ideal logarithmic layer. An obvious feature of the low Reynolds number case is that the viscous sublayer represents a notable share of the boundary layer, while this layer is not visible for the high Reynolds number cases. Above the viscous sublayer, the theoretical profile shows a near-constant value for κ up to $z^- \approx 0.1$ for the case Re1 and up to $z^- \approx 0.12$ for the cases Re2 and Re3. The difference in heights is a consequence of the increased scale separation between inner and outer layer for large \mathbf{Re} . In order to estimate κ_{LES} from the simulations, we perform a linear regression between the mean velocity in x -direction and the logarithm of the height between the seventh grid point and the grid point corresponding to the height $z^- = 0.1$ for $Re1_X$ and $z^- = 0.12$ for $Re2_X$ and $Re3_X$. We consider only points above the 7th grid point following arguments of Maronga et al. [2020b],

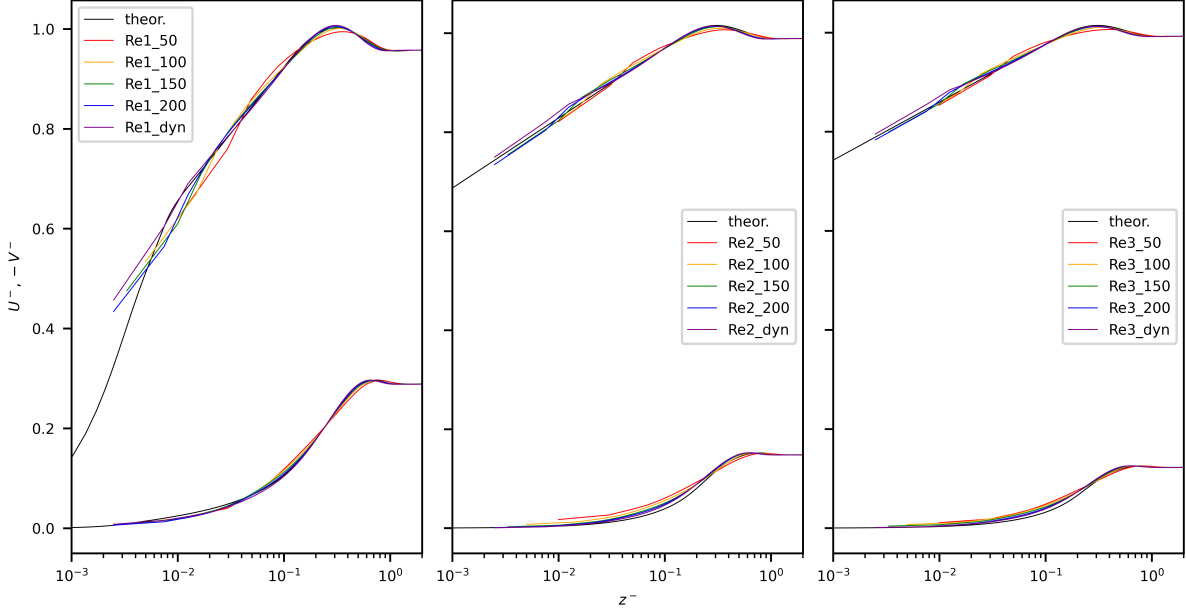


Figure 3: Shear-aligned velocity profiles in outer scaling. Solid lines: u -component, dashed lines: v -component

that in PALM, the mean velocity profiles follow MOST above the seventh grid point. [Why should we leave out the grid points below? After all, also the profile below the 7th grid point is what we get as LES result. Just leave out lowest three or four points to skip the obvious jumps? Above 7 the profiles smoothens. Actually, we get much better results for κ , when using all points in logarithmic layer] The number of values for each regression is 0, 6, 12, and 18 for ReX_50 , ReX_100 , ReX_150 and ReX_200 , respectively. Obviously, we do not compute κ for the coarsest simulations since there are only six grid points below $z^- \approx 0.12$. As can be seen in fig. 3, no layer with a constant gradient can be identified in the logarithmic plot for ReX_50 . The resulting κ_{LES} for the other simulations are shown in Tbl. 3. The coefficient of determination is above 0.99 for all fits. All Re have in common that κ_{LES} is decreasing with finer resolution. While the values for ReX_100 are rather high with a value around 0.53, finer resolution leads to more realistic values around 0.46 for $Re1_200$ and around 0.44 for $Re2_200$ and $Re3_200$. The dynamic subgrid closure yields lower values for κ_{LES} : in $Re1_dyn$ we even see $\kappa_{LES} = 0.39$, while $Re2_dyn$ and $Re3_dyn$ yield 0.42 and 0.43, respectively. All cases have in common that an increase in resolution leads to a profile of the Kármán measure closer to the theoretical curve. Above the first grid points, where the Kármán measure jumps between the values, the curve smoothens and approaches the expected value of κ (at least for the finer resolutions).

Fig. 5 shows the Kármán measure over the vertical grid index instead of the height. It illustrates that the course of the Kármán measure over the first layers is heavily influenced by the grid cell size Δ . Moreover, it shows that the kinks in the Kármán measure diminish around the seventh grid point for all simulations, in accordance with the observations of Maronga [2014] and Maronga and Reuder [2017]. Above the seventh grid point, the profile is no longer influenced by the size of the grid cells and becomes relatively constant. Exceptions are the simulations ReX_50 , where no constant κ can be observed.

As expected for an LES with isotropic grid spacing, the resolution near the surface is a critical part of the simulation. We can support our above observations by taking a look on the two-point correlation in the critical layers of the simulations. The two point correlation is

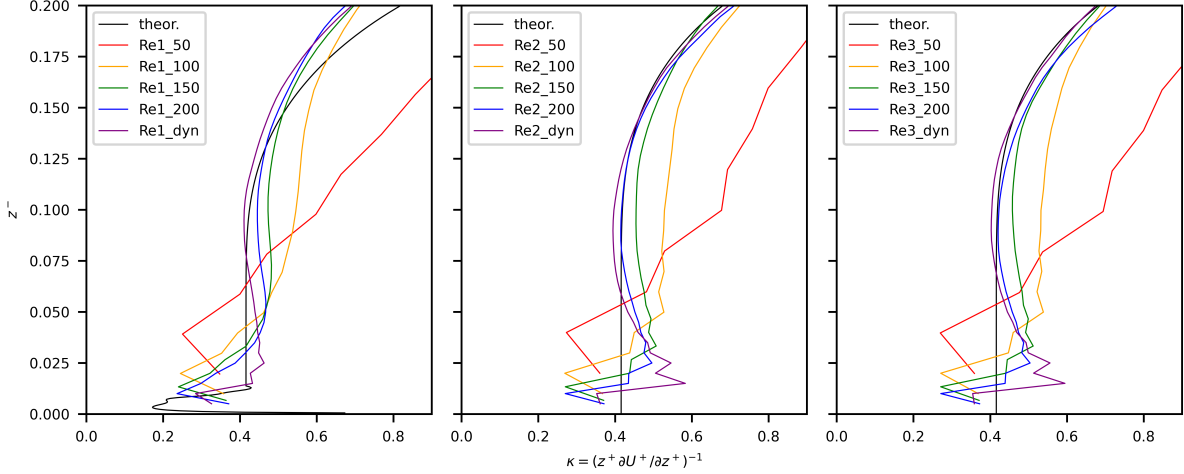


Figure 4: Kármán measure κ in the logarithmic region and above for different Reynolds numbers and resolutions

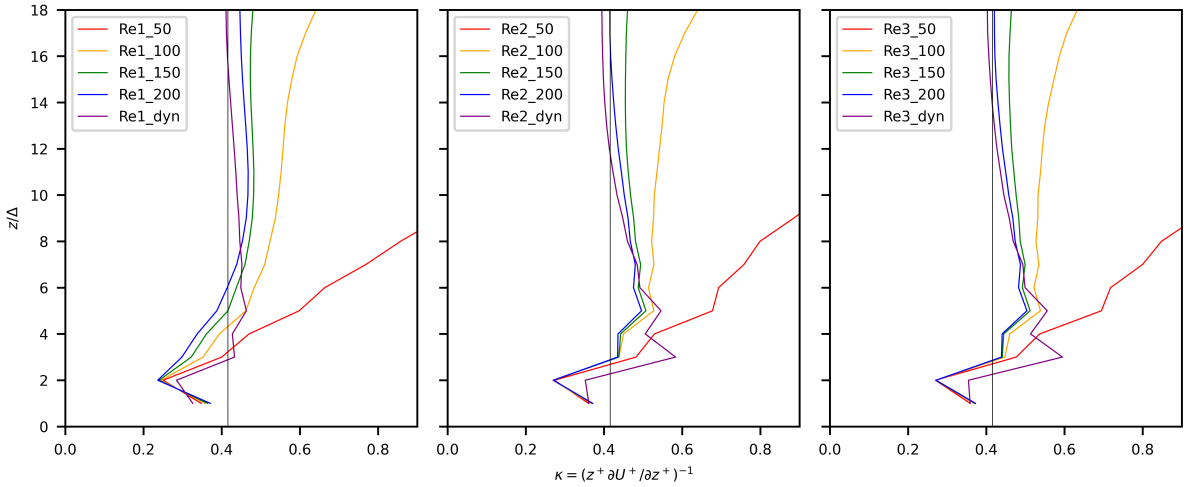


Figure 5: Kármán measure κ of the first grid points for different Reynolds numbers and resolutions

defined as

$$B_{xx}(x^*) = \langle u(x - x^*) u(x) \rangle / \sigma_u^2. \quad (22)$$

As suggested by Wurps et al. [2020], in an isotropic grid with periodic horizontal boundary conditions the turbulent structures of the velocity's w-component in y-direction can serve as an indicator how well the flow is resolved. Figure 6 shows the two-point correlation $B_{ww}(y^*)$ in a height of $z^- \approx 0.08$, which is right inside of the logarithmic layer. We define the average size of a structure in the flow σ as the distance where the two-point correlation drops to 0.3 (horizontal line in figure). The number of cells by which the average structure is resolved is equal to σ/Δ . All **Re** show a similar behaviour: the average size of the structure decreases with finer resolution and seems to approach a limit. The structure size of ReX_150 and ReX_200 are very close together, which indicates beginning convergence. Furthermore, the number of cells by which the structures are resolved exceed 4 from the resolution of ReX_150 on. This corresponds to the rule of thumb given in Wurps et al. [2020], that in a sufficiently resolved part of an LES the

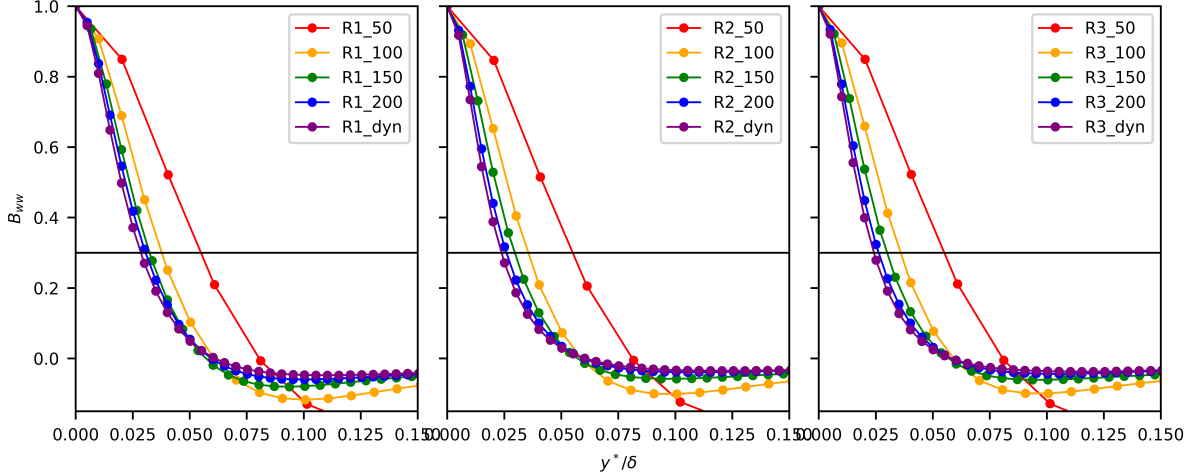


Figure 6: Two-point correlation of w-component in y-direction at $z^- \approx 0.08$. The horizontal line is at $B_{ww} = 0.3$

average structures of the w-component in y-direction should be resolved by at least 4 cells. The dynamic closure shows structures that are slightly smaller than the structures of ReX_200 .

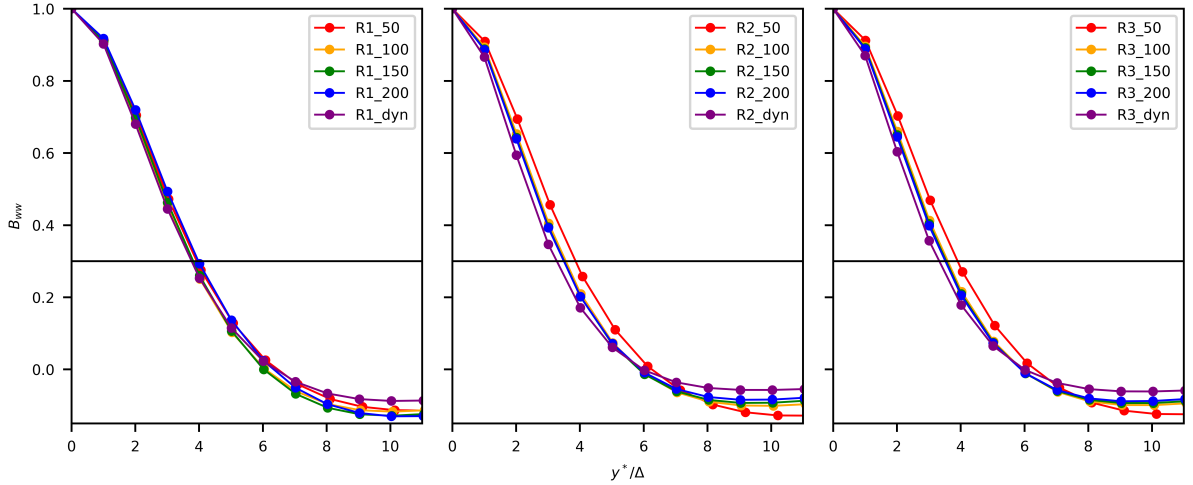


Figure 7: Two-point correlation of w-component in y-direction at the 8th grid point above the surface

Figure 7 shows $B_{ww}(y^*)$ at the 8th grid point above the bottom. Hence, the corresponding heights differ between the simulations, that is $z^- = 0.16, 0.08, 0.53, 0.04$ for ReX_50 , ReX_100 , ReX_150 , ReX_200 , respectively. For $Re1$, the curves almost collapse perfectly while for $Re2$ and $Re3$ we see slightly larger structures for ReX_50 and slightly smaller structures for ReX_dyn . This means that even 8 points above the lower boundary the smallest size of the turbulent structures rather depends on the grid cell size than on the actual height above the ground. According to the above findings and Maronga [2014], the flow should start to be well resolved from here on (above the seventh grid point). And indeed, the number of resolving cells is very close to 4 for $Re1$ and between 3 and 4 for $Re2$ and $Re3$, which does not fit exactly, but is close to the recommended 4 cells.

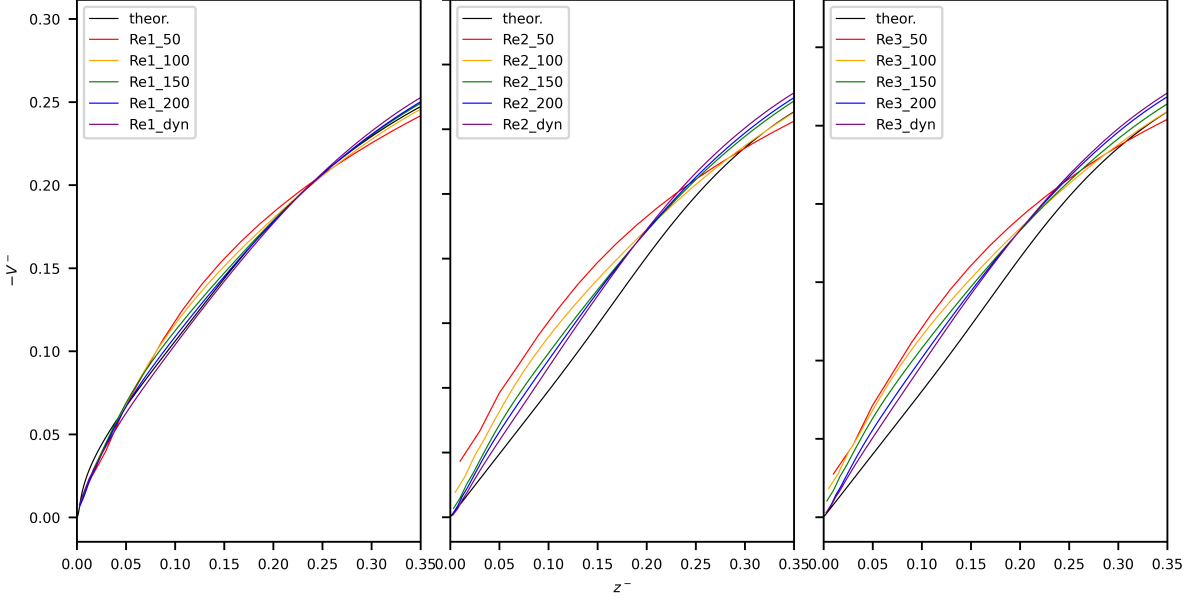


Figure 8: Span-wise velocity component in outer scaling

4.3 Logarithmic layer span-wise velocity

Figure 8 shows the span-wise velocity component in the lower part of the boundary layer. In the lowest part of $Re1$, a part of the viscous layer is visible. This velocity in this part is slightly underestimated by the the LES. Above, the simulations $Re1_200$ and $Re1_200$ are very close to the theoretical curve. Lower resolution leads to an overestimation of the velocity in the logarithmic layer. Around $z^- = 0.25$, while blending into the Ekman layer, the curves cross each other and the coarse simulations underestimate the velocity. For the higher Re all simulations overestimate the velocity in the logarithmic layer, while the coarser resolution leads to a higher velocity and finer resolution leads to a lower velocity and better agreement with the theoretical curve. Again, we see a crossing of the curves, but a little lower (between $z^- = 0.2$ and $z^- = 0.25$). A possible explanation of the fast increase of the steeper course of the coarser simulations is that the layers are coupled via less cells. [explanation?]

The mean wind direction in a specific layer depends on the balance of the pressure force and the Coriolis force as well as turbulent influence from layers above and below.

4.4 Ekman layer

Above the logarithmic layer, the Ekman layer follows, including most of the change of wind direction. The course of the wind velocity vector is visualized by hodographs, as plotted in fig. 2. The hodograph of $Re1_X$ is followed quite closely by all resolutions. Hence, all simulations – even $Re1_50$ – are resolved sufficiently to closely capture the course of the wind vector in the Ekman layer. The higher Re behave differently in the sense that the hodographs lie inside of the theoretical hodograph. An increased resolution ensures that at least the lowest grid point approaches the hodograph while the course of the hodograph's upper right part still does not reach the theoretical curve. [How can we explain this?]

In plot of the hodograph, the cross indicates the lowest grid point and the plus indicates the height where the velocity for the boundary condition is taken from. To avoid taking a velocity from the first layer of the simulation, where the turbulent flow is poorly resolved layer, we took the horizontal velocity near $z^- = 0.1$, where the mean velocity already veered away from the direction of the surface stress by around $\alpha/3$. However, the veering does not seem to negatively influence the resulting stress at the bottom: all but the coarsest resolutions yield a characteristic

velocity u_* that is very close to the theoretic value.

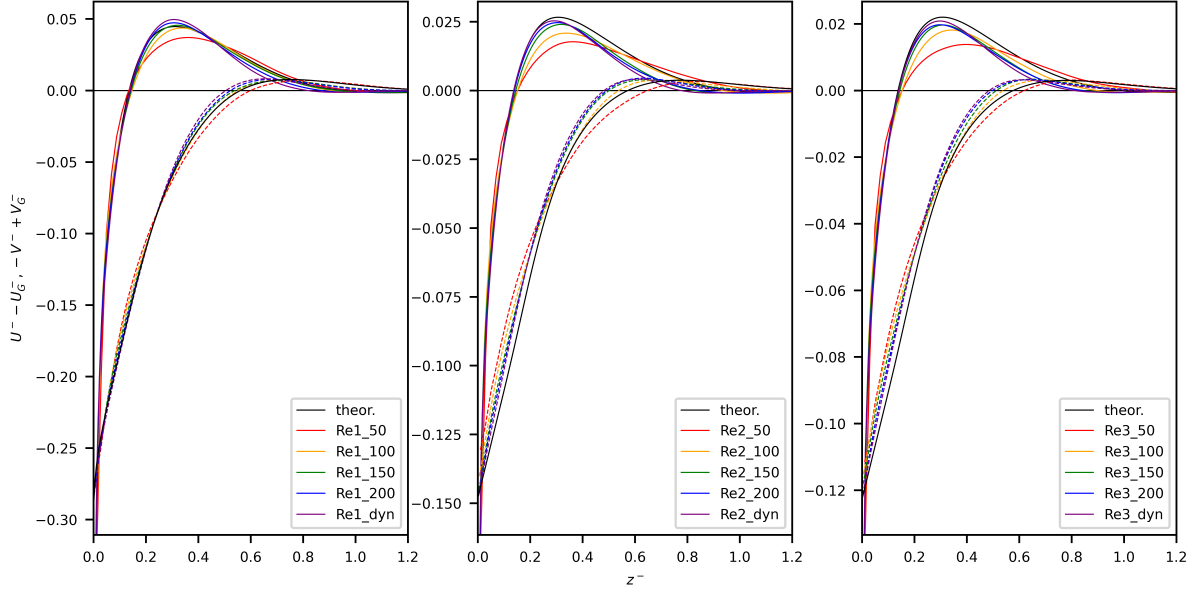


Figure 9: Shear-aligned velocity deficit in outer scaling. Solid lines: U-component, dashed lines: V-component

Figure 9 shows the shear-aligned velocity deficit of the whole boundary layer, the largest part of which is the Ekman layer. The strongest deviations from the theoretical profiles can be seen for the coarsest LES near the super-geostrophic maximum of the U-component. Finer resolution leads to a very good agreement with the extent of the maximum. However, for $Re2$ and $Re3$, the maximum velocity in x-direction is still not reached by the LES and the approach of the geostrophic wind in the upper part of the boundary layer takes place at lower heights than in theory. This is even more obvious for the V-component, where the maximum value is at a significantly lower height than in the theoretical curve. In general, a finer resolution leads to a lower maximum. [explanation?] The maximum at lower heights might also explain the too high velocities in the logarithmic layer for the higher Re .

[Include DNS data for $Re1$ to show a direct comparison between DNS and LES]

5 Discussion and Conclusions

As stated before, eq. 3 is very well validated for the range $400 < Re_D < 1600$ [Ansorge and Mellado, 2014]. For Reynolds numbers like $Re_D = 1.5 \times 10^5$ or even $Re_D = 10^6$, there exist neither DNS nor experimental data. Hence, the solutions of eq. 3 are not to be taken as certainly correct and one might assume that the LES solution is not definitively incorrect, even when we see big discrepancies between LES and model. However, the velocity profiles match so well that the LES results can be considered a confirmation of the theoretical curves.

[misalignment between stress and mean velocity: how big on the grid size scale]

The simulations $Re2_X$ and $Re3_X$ resolve only the largest scales (which is the intention of LES). But this implies that a refined grid leads to a better resolution of intermediate scales which might contribute significantly to the dynamics of the turbulent flow. This includes also the dynamics in the Ekman layer, where the mean direction of the flow is turning, so a finer resolution yields greater angles α_* . In different words: the setups of all Re use similar grid sizes in terms of the outer scale ($\Delta^- = \Delta/\delta = const.$) but different grid sizes in terms of the inner scale ($\Delta^+ = \delta^+ \cdot const. = Re_\tau \cdot const.$). This means that the inner and outer scales are much further apart for higher Reynolds numbers, so there are left more unresolved scales. Hence, a

refined resolution has a greater impact on the simulation. In this context, the case Re1_50 is quite interesting. From the inner perspective, it is much better resolved than all simulations of *Re2* and *Re3* but the simulation is not capable to capture the Ekman spiral properly. This is due to a poor resolution from the outer perspective, which is only 50 grid levels inside the whole boundary layer (≈ 30 grid levels below δ_{95}). Hence, a “well resolved” LES of the turbulent Ekman flow needs to be well resolved in terms of inner scaling as well as outer scaling.

Overall: good fit between theoretical profile and LES

Resolution of LES matters a lot [Sufficient resolution is needed to resolve the transition from outer to inner scale.]

The resolution ReX_150 resolves well the boundary layer in agreement with the findings of Wurps2019 where the neutral simulation was well resolved with more than 100 grid levels inside of the boundary layer δ_{95} . The ratio δ_{95}/δ is roughly 2/3 (slightly decreasing with Reynolds number). Hence, 150 grid levels within δ mean around 100 grid levels within δ_{95} .

Helpful for rating LES profile: height where profile should deviate from logarithmic shape.

Theoretical profiles provide a very detailed benchmark for all aspects of the flow. A very good hit of the hodograph might coincide with a poor curve for κ .

References

- Cedrick Ansorge and Juan Pedro Mellado. Global intermittency and collapsing turbulence in the stratified planetary boundary layer. *Boundary-layer meteorology*, 153(1):89–116, 2014.
- James G Brasseur and Tie Wei. Designing large-eddy simulation of the turbulent boundary layer to capture law-of-the-wall scaling. *Phys Fluids*, 22(2):021303, 2010.
- S-P Breton, J Sumner, Jens Nørkær Sørensen, Kurt Schaldemose Hansen, Sasan Sarmast, and Stefan Ivanell. A survey of modelling methods for high-fidelity wind farm simulations using large eddy simulation. *Philosophical Transactions of the Royal Society A: Mathematical, Physical and Engineering Sciences*, 375(2091):20160097, 2017.
- GT Csanady. On the “resistance law” of a turbulent ekman layer. *Journal of Atmospheric Sciences*, 24(5):467–471, 1967.
- James W Deardorff. Stratocumulus-capped mixed layers derived from a three-dimensional model. *Boundary-Layer Meteorology*, 18(4):495–527, 1980.
- I Esau. Simulation of ekman boundary layers by large eddy model with dynamic mixed subfilter closure. *Environmental Fluid Mechanics*, 4(3):273–303, 2004.
- C García-Sánchez, J van Beeck, and C Gorlé. Predictive large eddy simulations for urban flows: Challenges and opportunities. *Building and Environment*, 139:146–156, 2018.
- Stefan Heinz. Realizability of dynamic subgrid-scale stress models via stochastic analysis. *Monte Carlo Methods Appl*, 14(4):311–329, 2008.
- Qingfang Jiang, Shouping Wang, and Peter Sullivan. Large-eddy simulation study of log laws in a neutral ekman boundary layer. *Journal of the Atmospheric Sciences*, 75(6):1873–1889, 2018.
- Soshi Kawai and Johan Larsson. Wall-modeling in large eddy simulation: Length scales, grid resolution, and accuracy. *Physics of fluids*, 24(1), 2012.
- Andrey Nikolaevich Kolmogorov. Dissipation of energy in the locally isotropic turbulence. In *Dokl. Akad. Nauk SSSR A*, volume 32, pages 16–18, 1941.

Helmut Kraus. *Grundlagen der Grenzschicht-Meteorologie: Einführung in die Physik der atmosphärischen Grenzschicht und in die Mikrometeorologie*. Springer, 2008.

Björn Maronga. Monin–obukhov similarity functions for the structure parameters of temperature and humidity in the unstable surface layer: Results from high-resolution large-eddy simulations. *Journal of the Atmospheric Sciences*, 71(2):716–733, 2014.

Björn Maronga and Joachim Reuder. On the formulation and universality of monin–obukhov similarity functions for mean gradients and standard deviations in the unstable surface layer: Results from surface-layer-resolving large-eddy simulations. *Journal of the Atmospheric Sciences*, 74(4):989–1010, 2017.

Björn Maronga, Sabine Banzhaf, Cornelia Burmeister, Thomas Esch, Renate Forkel, Dominik Fröhlich, Vladimir Fuka, Katrin Frieda Gehrke, Jan Geletič, Sebastian Giersch, et al. Overview of the palm model system 6.0. *Geoscientific Model Development*, 13(3):1335–1372, 2020a.

Björn Maronga, Christoph Knigge, and Siegfried Raasch. An improved surface boundary condition for large-eddy simulations based on monin–obukhov similarity theory: evaluation and consequences for grid convergence in neutral and stable conditions. *Boundary-Layer Meteorology*, 174(2):297–325, 2020b.

Paul J Mason and David J Thomson. Stochastic backscatter in large-eddy simulations of boundary layers. *Journal of Fluid Mechanics*, 242:51–78, 1992.

D Mehta, AH Van Zuijlen, B Koren, JG Holierhoek, and H Bijl. Large eddy simulation of wind farm aerodynamics: A review. *Journal of Wind Engineering and Industrial Aerodynamics*, 133:1–17, 2014.

Wim Munters, Charles Meneveau, and Johan Meyers. Shifted periodic boundary conditions for simulations of wall-bounded turbulent flows. *Physics of Fluids*, 28(2), 2016.

AM Obukhov. On the distribution of energy in the spectrum of turbulent flow. *Bull. Acad. Sci. USSR, Geog. Geophys.*, 5:453–466, 1941.

Michael Optis, Adam Monahan, and Fred C Bosveld. Moving beyond monin–obukhov similarity theory in modelling wind-speed profiles in the lower atmospheric boundary layer under stable stratification. *Boundary-layer meteorology*, 153(3):497–514, 2014.

Fernando Porté-Agel, Yu-Ting Wu, Hao Lu, and Robert J Conzemius. Large-eddy simulation of atmospheric boundary layer flow through wind turbines and wind farms. *J Wind Eng Ind Aerodyn*, 99(4):154–168, 2011.

Philippe R Spalart. Theoretical and numerical study of a three-dimensional turbulent boundary layer. *Journal of Fluid Mechanics*, 205:319–340, 1989.

Philippe R Spalart, Gary N Coleman, and Roderick Johnstone. Direct numerical simulation of the ekman layer: A step in reynolds number, and cautious support for a log law with a shifted origin. *Physics of Fluids*, 20(10):101507, 2008.

Rob Stoll, Jeremy A Gibbs, Scott T Salesky, William Anderson, and Marc Calaf. Large-eddy simulation of the atmospheric boundary layer. *Boundary-Layer Meteorology*, 177:541–581, 2020.

H Tennekes. The logarithmic wind profile. *Journal of the Atmospheric Sciences*, 30(2):234–238, 1973.

Hauke Wurps, Gerald Steinfeld, and Stefan Heinz. Grid-resolution requirements for large-eddy simulations of the atmospheric boundary layer. *Boundary-Layer Meteorology*, 175(2):179–201, 2020.

6 stuff

In outer scaling, the length of the profiles regarding z^- of the LES is identical for all **Re**. This is due to the fact that for all simulations the ratio between boundary layer height and grid size δ/Δ is identical, which means that the profiles start at the same $z^- = 0.5\delta/200$.

A principal idea behind LES is to resolve only the large eddies of the flow, which carry most of the turbulent kinetic energy, and to model the small scales of the flow. The first grid point of an LES usually lies inside of the logarithmic region of the boundary layer; in fact – irrespective of computational feasibility constraints – this is also required for the MOST closure at the surface to remain valid (cf. Sec. 3.2).